ADVANCED OPTICAL MATERIALS
www.advopticalmat.de

Crystallization Modulation and Defect Passivation of Tin-Based Perovskite Light-Emitting Diodes Avoiding DMSO

Shun Tian, Oliver Nagy, Binbin Zhou, Ilhan Yavuz, Roland C. Turnell-Ritson, Yuxin Liu, Shengnan Zuo, Eva Unger, Antonio Abate, Guixiang Li, Xiao-Xin Gao, Peter Uhd Jepsen, Mohammad Khaja Nazeeruddin, and Paul J. Dyson**

Tin (Sn)-based perovskites are promising materials for perovskite-based light-emitting diodes (PeLEDs) that avoid toxic lead. However, the performance of Sn-based PeLEDs lags behind that of their lead analogues due to uncontrolled crystallization, the susceptibility of Sn(II) to oxidation, and high defect densities. In this study, ammonium thiocyanate (NH_4SCN) is used as an additive in DMSO-free perovskite precursor solution to afford Sn-based perovskites that are evaluated in PeLEDs. NH_4SCN modulates the crystallization process in the solution phase to improve the morphology and crystallinity of the resulting 2D perovskite films and inhibits the oxidation of Sn(II) to Sn(IV), a problem observed in DMSO. Transient terahertz spectroscopy reveals that NH_4SCN-based perovskite films have a higher free carrier density compared to the control films, indicative of reduced defect density. Consequently, pure-red Sn-based PeLEDs with an emissive peak of 629 nm achieve an external quantum efficiency of ≈1.4%, with an operating half-life of >11 min. These findings provide valuable insights into the preparation of lead-free perovskite materials avoiding DMSO for application in optoelectronic devices.

1. Introduction

Solution-processed halide perovskites have attracted great attention in light-emitting diodes (LEDs) because of their excellent optoelectronic properties.[1,2,3] Although the external quantum efficiencies (EQEs) of lead-based halide perovskite LEDs (PeLEDs) have exceeded 20%,[4,5] the toxicity of lead could cause environmental and health problems if deployed on large scales. Therefore, developing low-toxicity Pb-free perovskites has become a necessary pathway, with attention focused on Sn-halide perovskites. However, the performance of Sn-based perovskite devices lags behind their lead analogues due to the fast and uncontrolled crystallization process, facile oxidation of Sn(II), and the generally poor morphologies of tin-based perovskite materials. Additionally, tin-based perovskites can be oxidized by the dimethyl sulfoxide (DMSO) solvent,[6,7] which is the usual solvent from which they are deposited. Moreover, the acidity of poly(3,4-ethylenedioxythiophene):poly(styrenesulfonate) (PEDOT:PSS), the most commonly used hole transport material in Sn-based perovskite devices, can potentially damage transparent conductive oxide electrodes and the tin-based perovskite crystal structure, which impairs long-term device stability.[8]

In order to alleviate the issues of Sn(II) oxidation and fast and uncontrolled crystallization, a variety of additives have been introduced into tin perovskite precursor solutions (PPSs), such as 2-imidodicarbonic diamide,[9] cyanuric acid,[10] valeric acid,[11] 2,7-bis(diphenylphosphoryl)-9,9′-spirobifluorene,[12] Vitamin B1,[13] triphenylphosphine,[14] thiourea[15] and 3-(aminomethyl) piperidinium,[16] etc. These additives effectively retard crystallization of perovskite clusters, through reversible coordination to the Sn centres, facilitating the formation of high-quality Sn-based perovskite films.[17] The improved film quality reduces losses from non-radiative recombination. Some of the additives are also reductants, inhibiting Sn(II) oxidation.[18] As a result, the performance of additive-treated Sn-based perovskite devices is enhanced. Although significant progress has been made in tin-based PeLEDs with peak EQEs over 10% using DMSO due to its strong coordination with Sn^{2+} species,[10,14,19,20] reports

S. Tian, R. C. Turnell-Ritson, G. Li, X.-X. Gao, M. K. Nazeeruddin, P. J. Dyson
Institute of Chemical Sciences and Engineering
École Polytechnique Fédérale de Lausanne (EPFL)
Lausanne 1015, Switzerland
E-mail: mdkhaja.nazeeruddin@epfl.ch; paul.dyson@epfl.ch

O. Nagy, B. Zhou, P. U. Jepsen
Department of Electrical and Photonics Engineering
Technical University of Denmark
Kgs. Lyngby 2800, Denmark

I. Yavuz
Department of Physics
Marmara University
Istanbul TR-34722, Türkiye

Y. Liu, S. Zuo, E. Unger, A. Abate
Helmholtz-Zentrum Berlin für Materialien und Energie GmbH
Kekuléstraße 5, 12489 Berlin, Germany

The ORCID identification number(s) for the author(s) of this article can be found under https://doi.org/10.1002/adom.202503684

DOI: 10.1002/adom.202503684

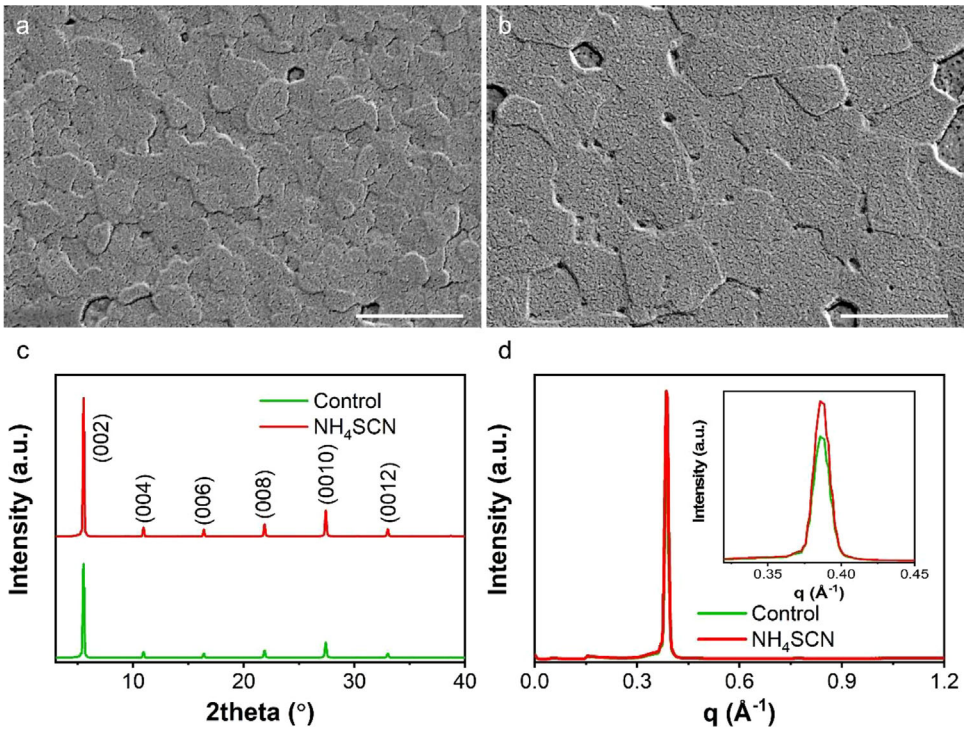

Figure 1. Top-surface SEM images of the a) control and b) NH_4SCN films on ITO/NiO_x/4PADCB substrates. Scale bar = 1 µm. c) XRD and d) GIWAXS patterns of the control and NH_4SCN films on ITO/NiO_x/4PADCB substrates.

on avoiding DMSO remain scarce. Developing tin-based perovskite optoelectronic devices with avoiding DMSO is of great importance, as it helps to mitigate the direct oxidation of Sn(II) species induced by DMSO. However, the alternative solvents avoiding DMSO can accelerate the crystallization process of tin perovskites, resulting in poor surface morphologies and an increase in defects.[21] Therefore, it is crucial to develop methods to modulate the crystallization process of tin perovskites, avoiding utilizing DMSO, aiming to improve the film quality of tin perovskites.

In this work, we prepared Sn-based perovskites from phenethylammonium iodide (PEAI), SnI_2, and SnF_2 (molar ratio 2:1:0.1) dissolved in a mixture of N,N-diethylformamide (DEF)/1,3-dimethyl3,4,5,6-tetrahydro-2(1H)-pyrimidinone (DMPU).[6,22][OBJ] DMSO is usually used to prepare tin PPSs, but it leads to Sn(II) oxidation so should be avoided.[6,7,22] Ammonium thiocyanate (NH_4SCN) was further employed as an additive in the tin PPS to modulate the crystallization/oxidation processes, as it has previously been shown to retard the perovskite crystallization process and improve the resulting film crystallinity for solar cell applications.[23,24,25] For example, coordination of SCN^- to SnI_2 can slow down the crystallization process of $CH(NH_2)_2SnI_3$ perovskite, improving film quality.[23] It has been shown that NH_4SCN separates the nucleation and growth processes of perovskite polycrystalline films to yield a 2D-quasi-2D-3D hierarchy structure.[25] NH_4SCN has also been shown to improve the crystallinity of low-dimensional layered lead-based perovskites, as evidenced by enhanced X-ray diffraction (XRD) intensities.[24,26] Solution phase nuclear magnetic resonance (NMR) spectroscopy shows that the NH_4SCN additive suppresses the oxidation of Sn(II) to Sn(IV) in PPSs. The enhanced crystallinity of the resulting 2D (PEA_2SnI_4) films was confirmed by XRD and grazing-incidence wide-angle X-ray scattering (GIWAXS). Ultrafast terahertz (THz) spectroscopy reveals that the enhancement of free carrier response in Sn-based perovskite films may be attributed to a decrease in defects rather than an increase in carrier mobility. NiO_x/(4-(7H-dibenzo[c,g]carbazol-7-yl)butyl)phosphonic acid (4PADCB) (self-assembled monolayer, SAM) was used as the hole transport layer, with the Sn-based perovskite, and a commercial electron transport material, 1,3,5-tris(1-phenyl-1H-benzimidazole-2-yl)-benzene (TPBi), to afford devices with the architecture glass/Indium tin oxide (ITO)/NiO_x/4PADCB/PEA_2SnI_4/TPBi/LiF/Al. The pure-red Sn-based PeLEDs employing NH_4SCN exhibit an enhanced EQE of 1.39%, compared to 0.32% for the control device. Additionally, the operational stability of the NH_4SCN modified PeLED is approximately four times longer than that of its control counterpart.

2. Results and Discussion

PPSs, films, or devices without an additive are denoted as control PPSs, films, or devices, whereas those containing the NH_4SCN additive are referred to as NH_4SCN PPSs, films, or devices. Control and NH_4SCN PPSs (see above and Supporting Information for their composition) were spin-coated on ITO/NiO_x/4PADCB substrates using toluene as antisolvent. The resulting films were annealed at 70 °C for 15 min in a N_2-filled glovebox. **Figure 1** a,b show the top-surface scanning electron microscopy (SEM) images of the control and NH_4SCN perovskite films, respectively. The surface of the control film contains numerous pinholes and grain boundaries where many defects tend to accumulate.

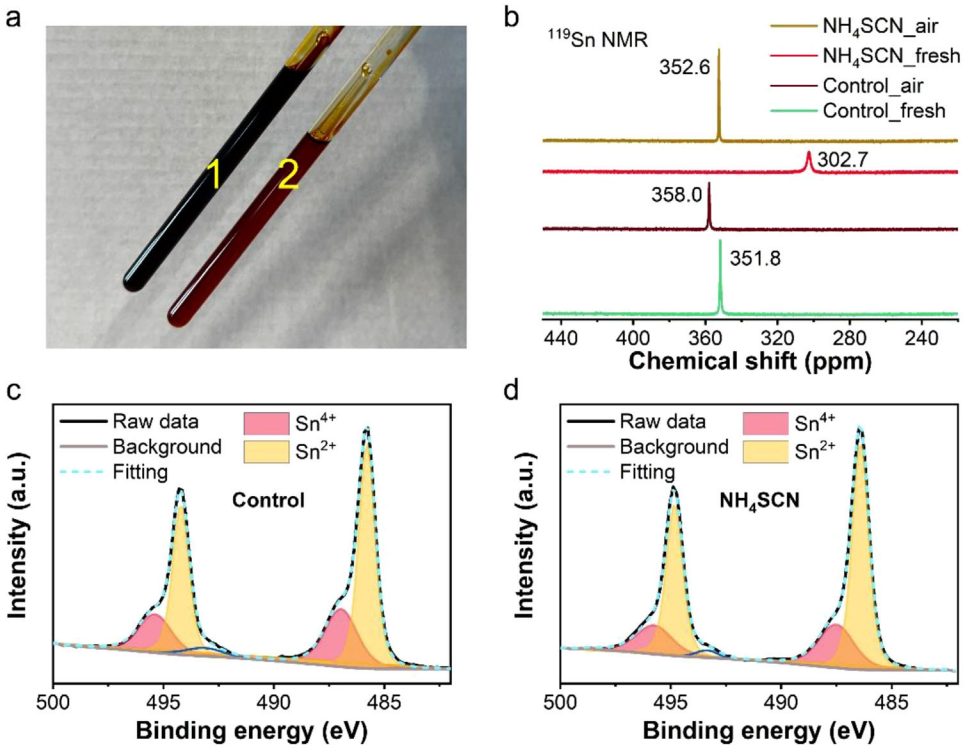

Figure 2. a) Photograph of the control and NH_4SCN PPSs after 1 h air exposure (relative humidity ≈25%) (the NH_4SCN:SnI_2 molar ratio is 0.6:1.0, the PPS concentration is 0.5 M.). Solutions numbered 1 and 2 represent control and NH_4SCN PPSs with air exposure. b) ^{119}Sn NMR spectra of the fresh and oxidized control and NH_4SCN PPSs. XPS spectra of the c) control and d) NH_4SCN tin perovskite films after exposure to air (relative humidity ≈20%) for 3 h.

Compared to the control film, the NH_4SCN film surface contains fewer pinholes and grain boundaries, and has larger average grain sizes (674 nm vs 338 nm), indicating enhanced film morphology and a slower crystallization process. The average grain size of the film with the NH_4SCN:SnI_2 ratio of 0.1:1 is 546 nm. Increasing the NH_4SCN:SnI_2 ratio to 0.5:1 results in an average grain size of 1135 nm, but this increase in grain size is accompanied by distinct cracks (Figure S1, Supporting Information). In addition to the improved morphology, the NH_4SCN additive should enhance the crystallinity of the film. Figure 1c shows the XRD patterns of the control and NH_4SCN films. Both films exhibit the typical patterns of 2D Sn-based perovskites, characterized by diffraction peaks along the (00l) direction (where *l* is 2, 4, 6, 8, 10, and 12). The NH_4SCN film does not exhibit any peak shifts, indicating that the NH_4^+ cations and SCN^- anions are not included in the crystal structure. The peak intensities of the NH_4SCN film are stronger than those of the control film, indicating the improved crystallinity of the NH_4SCN film. GIWAXS was employed to further explore the effects of NH_4SCN-doping on the perovskite crystallization process (Figure S2, Supporting Information), with a grazing incidence angle of 2.0°. The 2D GIWAXS patterns show that both perovskite films exhibit clear Bragg spots rather than Debye–Scherrer rings, indicating that they are oriented parallel to the substrates. This phenomenon is consistent with the GIWAXS pattern of the reported pure PEA_2PbI_4 film.[27] Furthermore, the integrated patterns indicate that the NH_4SCN film exhibits a stronger intensity along the (002) crystal plane at $q = 0.38$ Å^{-1} compared to the control film in Figure 1 d, suggesting a preferred orientation.[28] The preferred crystalline orientation indicates a reduction in defects within the perovskite film, which in turn reduces non-radiative recombination. The Debye–Scherrer rings at $q_z \approx 2.0$ Å^{-1} in Figure S2 (Supporting Information) may be attributed to the ITO. The cross-sectional SEM images illustrate that the thickness of the control and NH_4SCN films is ≈40.0 ± 3.5 nm (Figure S3, Supporting Information). The NH_4SCN film has better vertical uniformity and horizontal continuity compared to the control film.

The 0.5 M fresh control and NH_4SCN PPSs were exposed to air for 1 h (relative humidity ≈25%). The colors of the PPSs change from yellow to black–red in the case of the control, and deep red in the case of the NH_4SCN PPS, (**Figure 2a**), indicating that some Sn^{2+} is oxidized to Sn^{4+}[6]. The ^{119}Sn NMR spectra of the fresh and oxidized tin PPSs are shown in Figure 2b. The Sn^{2+} chemical shift of the fresh control PPS is 351.8 ppm, which shifts slightly downfield of 358.0 ppm due to a decrease in Sn^{2+} concentration after air exposure, i.e., Sn^{2+} is oxidized to Sn^{4+}. Compared to the fresh control PPS, the intensity of the Sn^{2+} signal in the oxidized control PPS reduces by ≈39.6%, which is consistent with the quantified proportion of Sn^{4+} species (37.91% in Table S1, Supporting Information) determined using the ^{119}Sn NMR spectra. The Sn^{2+} signal of the fresh NH_4SCN PPS is shifted upfield relative to the fresh control PPS to 302.7 ppm, indicating that SCN^- anions interact with the Sn^{2+} cations. The density functional theory (DFT) calculation results show that SCN^- could form more stabilized interactions with SnI_2 via its S atom than N atom (Figure S4, Supporting Information). Charge analysis

was used to quantify the amount of electron density from SCN^{2-} accepted by the Sn^{2+} center following coordination through either the N atom or S atom. When the Sn^{2+} center coordinates with SCN^- via the N atom, Sn^{2+} accepts ≈0.14e whereas SCN^- donates 0.38e. In contrast, Sn^{2+} accepts 0.22e while SCN^- donates 0.42e when the Sn^{2+} center coordinates with SCN^- via the S atom. This quantitative charge donation–acceptance interaction is consistent with the calculated interaction energies (−0.815 eV for N-binding and −0.987 eV for S-binding), confirming that SCN^- preferentially coordinates to the Sn^{2+} center, with slightly stronger stabilization through S-binding. The electron density difference plots in Figure S5 (Supporting Information) further illustrate the coordination between SCN^- and Sn^{2+}. These visual results complement the charge analysis and interaction energies, showing that SCN^- donates electron density to Sn^{2+} upon coordination, with slightly stronger stabilization in the S-bound case. Compared to the fresh PPS, the intensity of the Sn^{2+} signal in the oxidized NH_4SCN PPS decreases by only 14.2%, suggesting that SCN^- retards the oxidation of Sn^{2+} in the PPS upon exposure to air. DFT calculations reveal that the SCN^- group lowers the net energy gain associated with SnO_2 formation, rendering full oxidation less thermodynamically favorable (Figure S6, Supporting Information). This result suggests that SCN^- may suppress the overall oxidation rate and extent by stabilizing intermediate states and diminishing the final exergonic driving force. Additionally, the FWHM of the fresh NH_4SCN PPS is significantly wider than that of the fresh PPS, further indicating interactions between the SCN^- and Sn^{2+}. The Sn^{2+} peak of the NH_4SCN PPS undergoes a large shift after air exposure relative to the fresh sample, being located between the Sn^{2+} chemical shift of the fresh and air-exposed control PPSs. This change further confirms that the Sn^{2+} peak shifts downfield due to a decrease in Sn^{2+} concentration upon air exposure and suggests that SCN^- preferentially coordinates with Sn^{4+} rather than Sn^{2+} in air-exposed PPSs. The coordination energies of Sn^{2+} and Sn^{4+} with SCN^- were calculated using DFT and the equation $E = E_{SnSCN} - (E_{Sn^{q+}} + E_{SCN^-})$. The results show that Sn^{2+} binds to SCN^- with an energy of -2.1 kcal mol^{-1}, whereas Sn^{4+} exhibits a much stronger coordination with an energy of -15.5 kcal mol^{-1}, indicating a much higher affinity of Sn^{4+} for SCN^-. Although SCN^- shows stronger binding affinity to Sn^{4+} thermodynamically, the solution-phase DFT calculations in DEF/DMPU (PCM) indicate that in the presence of SCN^-, the oxidation of Sn^{2+} to Sn^{4+} is less favorable and kinetically hindered (Figure S7, Supporting Information). Coordination of SCN^- to Sn^{2+} reduces the thermodynamic driving force for oxidation. The SCN^- anions may facilitate initial electron transfer or local rearrangements by lowering kinetic barriers, yet it simultaneously hinders oxygen adsorption and diffusion, which are likely to become the rate-limiting steps. Therefore, Sn^{2+} oxidation is limited not by electron transfer but by oxygen access or subsequent reorganization, indicating that kinetic inhibition combines with thermodynamic stabilization to suppress oxidation. This also suggests a mechanism by which NH_4SCN could slow down the crystallization of tin perovskites, leading to reduced grain boundaries and enhanced crystallinity of the perovskite films. A $[SnI_4(DEF/DMPU)_2]$ signal could be detected in both air-exposed control and NH_4SCN PPSs, with a peak at −2150.5 ppm (Figure S8 a, Supporting Information). The ^{119}Sn NMR spectrum of the NH_4SCN PPS following exposure to air contains 6 peaks that may be attributed to Sn^{4+} species (Figure S8, Supporting Information). The total quantified proportion of the 6 Sn^{4+} species in the NH_4SCN PPS is ≈12.2 % relative to the total Sn species (Table S1, Supporting Information), which is consistent with the value obtained from Figure 2 b. The ^{119}Sn NMR spectra of the NH_4SCN, NH_4I, and control PPSs contain peaks at 321.9, 350.9, and 352.2 ppm, respectively. The shift in the peak of the NH_4SCN PPS relative to the control PPS is larger than that of the NH_4I PPS relative to the control PPS, suggesting that the SCN^- anion interacts more strongly with the Sn^{2+} ion compared to the I^- anion (Figure S9, Supporting Information). Moreover, the difference between the peaks for the NH_4SCN and PEASCN PPSs is comparatively small, i.e., 2.3 ppm, indicating a negligible influence of PEA^+ and NH_4^+ cations on Sn^{2+} ions, as expected. Hence, the ^{119}Sn NMR spectra of the PPSs support the DFT calculations, which indicate that the binding of SCN^- to Sn^{2+} impedes oxidation to Sn^{4+}. The color of control PPS in DMSO changed from yellow to red upon heating at 70 °C for 80 h, suggesting the formation of Sn(IV) species (Figure S10 a,b, Supporting Information),[6] whereas in DEF/DMPU the color remains unchanged. ^{119}Sn NMR spectra reveal the presence of Sn(IV) species in DMSO after heating, whereas no such signals are observed in DEF/DMPU (Figure S10 c, Supporting Information). Therefore, avoiding DMSO prevents or retards the intrinsic oxidation of Sn(II) species.

X-ray photoelectron spectroscopy (XPS) was used to analyze the elemental compositions of the tin perovskite film surfaces. The Sn(II):Sn(IV) ratio on the surface of the fresh control film (96.3:3.7) is slightly lower than that of the fresh NH_4SCN film (97.6:2.4) (Figure S11, Supporting Information). Subsequently, the fresh control and NH_4SCN films were exposed to air (relative humidity ≈20%) for 3 h. The Sn(II):Sn(IV) ratio of the control film is 66.5:33.5 (Figure 2c), which is higher than that of the NH_4SCN film (71.8:22.8) (Figure 2d), indicating that NH_4SCN films are more stable in air. However, no S 2p XPS signal is found on the NH_4SCN film surface, implying that SCN^- is not localized on the film surface, as observed previously.[29] XPS depth profiling was carried out to investigate the SCN^- ion distribution along the vertical direction in the NH_4SCN film. The depth profiles for S 2p and Ni 2p signals were obtained by alternating cycles of argon ion sputtering with an ion energy of 2 KeV and each etching time lasting 15 s. At the surface (no sputtering), there is no S 2p signal (Figure S12 a, Supporting Information). With increasing sputtering cycles, the S 2p signal was not detected throughout the whole film thickness, however, accompanied by an increase in the Ni 2p signal with the binding energy of 853.2 eV (Figure S12 b, Supporting Information).

For a comprehensive study of the crystallization process of tin perovskites, the in situ PL measurements were carried out for recording the evolution of the control and NH_4SCN films (Figure S13, Supporting Information). The PL heatmaps of the control and NH_4SCN films during spin-coating are shown in Figure S13 a,b (Supporting Information). Upon addition of the antisolvent at ≈12 s, the PL signal of the control film immediately appear, whereas a slight delay was observed for the NH_4SCN film. The PL intensity of the control and NH_4SCN films increases rapidly within the following 8 s (Figure S13 c, Supporting Information), implying fast nucleation of perovskite crystals. This rapid nucleation was induced by supersaturation resulting from

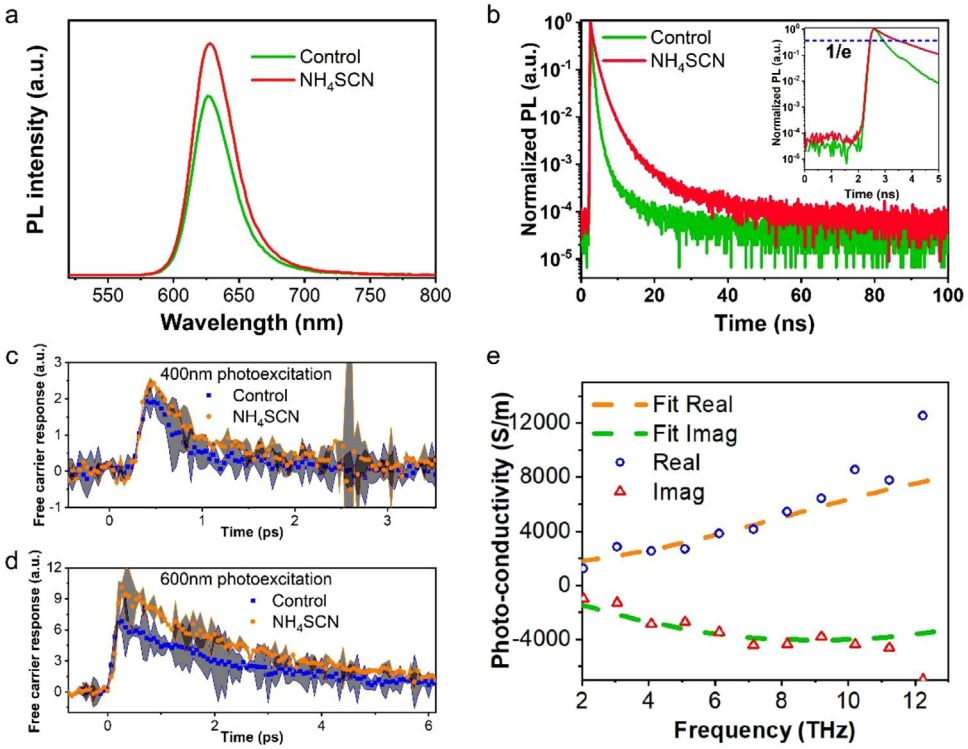

Figure 3. a) PL and b) TRPL spectra of tin perovskite films with or without NH_4SCN on ITO/NiO_x/4PADCB substrate. Average 1D response of the control and NH_4SCN films under c) the 400 nm optical excitation and d) 600 nm optical excitation, with the standard deviation represented by the shadow region (each condition has 6 measurements). e) Extracted frequency-dependent complex photoconductivity of the NH_4SCN film and its Drude–Smith fit.

solvent extraction by the antisolvent.[30,31] After 20 s, the PL intensity of the control and NH_4SCN films increases almost linearly due to crystal growth, and the NH_4SCN film exhibited higher PL intensity compared to the control film. The PL peaks of the control (618 nm) and NH_4SCN (624 nm) films remain stable during the spin-coating process due to the pure phase property of 2D tin perovskite (Figure S13 d, Supporting Information), which differs from the red-shifted trend in 2D/3D mixed perovskites.[20,31] The NH_4SCN film has a longer PL peak wavelength compared to the control film, which may be attributed to the larger grain size.

Based on the above study, tentative nucleation and crystallization processes of control and NH_4SCN PPSs are proposed. The spontaneous formation of edge-sharing SnI_2 nanocrystals in DEF/DMPU solution has been proposed to result in uneven nucleation, as nuclei are formed immediately upon addition of the antisolvent, and the subsequent rapid growth of these nuclei leads to the creation of numerous pinholes and a poor morphology.[32] The NH_4SCN interacts with SnI_2, likely inhibiting the rate of film crystallization as proposed previously,[23] promoting ordered growth and yielding films with large grain size and fewer pinholes. The slower crystallization leads to a more uniform nucleation, improved film morphology, and reduced defects.[11]

The coordination of SCN^- to Sn^{2+} in solution modulates the perovskite crystallization process and retards Sn^{2+} oxidation, thereby significantly enhancing the optical properties of the resulting perovskite films. As shown in **Figure 3** a, the NH_4SCN film on ITO/NiO_x/4PADCB substrate exhibits increased steady-state photoluminescence (PL) intensity compared to the control film. Consequently, the NH_4SCN film exhibits a prolonged transient PL lifetime, increasing from 0.34 ns in the control film to 0.88 ns (Figure 3b), confirming reduced non-radiative recombination. The photoluminescence quantum yields (PLQYs) of the control and NH_4SCN films deposited on quartz substrates is shown in Figure S14 (Supporting Information). The NH_4SCN films exhibit higher average PLQY values compared to the control films (3.8% vs 1.2%), suggesting that trap-assisted non-radiative recombination is suppressed in the films.

Transient optical-pump THz-probe spectroscopy (OPTP) was employed to investigate the ultrafast dynamics of photoexcited tin perovskite films. The OPTP techniques have been widely used to investigate ultrafast carrier dynamics in perovskite thin films and crystals, particularly in the context of fundamental material research and in solar cell research.[33,34] This technique has been rarely applied to actual perovskite LEDs. However, the carrier dynamics and photoconductive properties probed by OPTP are highly relevant to PeLED performance. These properties – such as carrier mobility, lifetime, and trap-assisted recombination – directly influence key device metrics, including internal quantum efficiency, charge balance, and operational stability. As such, transient THz spectroscopy provides useful insights into the physics of the emissive layer, potentially guiding the design and optimization of high-performance PeLEDs. Ultra-broadband THz pulses were used in a reflection geometry, enabling time-resolved probing of photocarrier dynamics within the first few picoseconds after photoexcitation.[35] Figure 3c,d shows the time

evolution of the overall free carrier response, observed as transient changes in THz wave reflection induced by photocarriers under 400 and 600 nm optical excitation, respectively. The duration of the excitation pulses was ≈40 fs. In both cases, the NH_4SCN films exhibit significantly stronger free-carrier responses than the control films. Under each of the optical excitation wavelengths, the response dynamics of the control and NH_4SCN films share a very similar shape, differing only in amplitude. This suggests that the photocarrier density or photocarrier mobility in the NH_4SCN tin perovskite film is enhanced, with the band structure remaining unchanged, which is consistent with SCN^- anions not being included in the perovskite structure. At both excitation wavelengths, the photocarrier response peaks of the films show ≈300 fs after photoexcitation. However, the subsequent recombination dynamics differ (as illustrated in Figure S15, Supporting Information). Under 600 nm excitation (corresponding to an energy slightly greater than the bandgap of the tin perovskites of 1.96 eV), the response exhibits a relatively slow, single-exponential decay. In contrast, under 400 nm excitation (much greater than the bandgap energy), the recombination occurs in two distinct stages comprising an initial rapid decay, attributed to hot carrier relaxation (likely non-radiative, as indicated by the PL spectra),[36] followed by a slower decay, resembling that observed in the 600 nm excitation case. Based on the PL spectra, this slower component is most likely due to radiative recombination from the conduction band minimum (CBM) to the valence band maximum (VBM) of the tin perovskite films.

2D transient THz spectroscopy was performed to determine both the free carrier density and carrier mobility in tin perovskite films during the first few picoseconds following photoexcitation. At each probe delay time τ_p, the reflected THz waveform under optical excitation $E_{pump}(\tau_p, t)$ was recorded. Simultaneously, the differential THz waveforms, defined as $\Delta E(\tau_p, t) = E_{pump}(\tau_p, t) - E_{ref}(t)$, were acquired, where $E_{ref}(t)$ represents the reference waveform without optical excitation. Fourier transforms of both $\Delta E(\tau_p, t)$ and $E_{ref}(t)$ were used to calculate the complex transient conductivity using Equation (1).

$$1 + \frac{\Delta E\left(\omega, \tau_p\right)}{E_{ref}\left(\omega\right)} = \left(\frac{1 - n_s - Z_0 d\tilde{\sigma}\left(\omega, \tau_p\right)}{1 + n_s + Z_0 d\tilde{\sigma}\left(\omega, \tau_p\right)}\right)\left(\frac{1 + n_s}{1 - n_s}\right) \quad (1)$$

The complex photoconductivity of the excited film, $\tilde{\sigma}(\omega, \tau_p) = \sigma_1(\omega) + i\sigma_2(\omega)$ was extracted using the thin-film approximation, where σ_1 and σ_2 represent the real and imaginary components, and ω denotes the angular frequency. Z_0 is the impedance of free space, d is the thickness of the photoexcited film, and n_s is the refractive index of the substrate. To fit the experimental data, we applied a phenomenological Drude–Smith model, expressed as Equation (2):

$$\tilde{\sigma}\left(\omega\right) = \frac{\omega_p^2 \varepsilon_0 \tau}{1 - i\omega\tau}\left(1 + \frac{c_1}{1 - i\omega\tau}\right) \quad (2)$$

where $\omega_p^2 = \frac{ne^2}{\varepsilon_0 m^*}$ is the plasma frequency, n is the free carrier density, τ is the carrier momentum relaxation time, and c_1 is the carrier back-scattering parameter (with $c_1 = -1$ representing fully localized response). From the 2D scans, the frequency-dependent complex conductivity spectra of the photoinduced charge carriers at various pump-probe delays were extracted. By fitting these spectra with the Drude–Smith model, key transport parameters, such as carrier density and mobility, were quantitatively determined as the DC conductivity (the low-frequency limit of conductivity) $\sigma_{DC} = \omega_p^2 \varepsilon_0 \tau(1 + c_1)$, mobility $\mu = e\tau/m^*$, carrier density $n = \frac{\sigma_{DC}}{e\mu(1+c_1)}$.[37] A representative photoconductivity spectrum together with simultaneous Drude–Smith model fits to σ_1 and σ_2 are shown in Figure 3e, obtained from the NH_4SCN films under 600 nm optical excitation, measured at 1.667 ps after the peak pump-probe delay (see Figure S16, Supporting Information for full THz measurement data). For the 2D spectroscopy analysis, a film thickness of 40 nm and an effective hole mass of 0.069 m_e were used.[38] Drude–Smitch fitting was applied to the frequency range of 2–10 THz to extract key electrical properties of the photo-induced transient charge carriers in the NH_4SCN films. From this analysis, the DC conductivity (the low-frequency limit of conductivity), photocarrier mobility, and carrier density were determined and are summarized in Table 1. The same fitting procedure was performed on the control films under identical experimental conditions, and their corresponding values are also presented in Table 1. The results show that the NH_4SCN films have a 29% increase in photocarrier density compared to the control films, whereas the carrier mobility remains nearly unchanged. This indicates that the observed enhancement in the free carrier response (as seen in Figure 3c,d) is primarily attributed to the increase in carrier concentration, rather than improved mobility. Notably, the higher photocarrier density in the NH_4SCN films is consistently observed across various pump-probe delay times. These findings suggest that the NH_4SCN additive effectively reduces defects in the tin perovskite film, thereby supporting more efficient generation and maintenance of free carriers.

Table 1. Extracted properties of the photoinduced carriers in the control and NH_4SCN films (1.667 ps after the peak pump-probe delay).

Film	σ_{DC} (S m^{-1})	n (10^{18} cm^{-3})	μ ($cm^2v^{-1}S^{-1}$)
NH_4SCN film	1551.8	6.92	179.94
Control film	801.8	5.36	170.29

Sn PeLEDs were fabricated using a device structure of glass/ITO/NiO_x/4PADCB/Tin perovskite/TPBi/LiF/Al (**Figure 4a**). Figure 4b shows the energy level diagram of the PeLEDs. The VBMs of NiO_x and 4PADCB were calculated to be −4.93 and −5.30 eV, respectively, as determined by ultraviolet photoelectron spectroscopy (UPS) (Figure S17, Supporting Information). The CBMs of NiO_x and 4PADCB were determined by adding their optical bandgaps[39,40] to their VBMs, with detailed energy level data summarized in Table S2 (Supporting Information). The VBMs of the control and NH4SCN perovskite films were measured to be −5.09 and −5.18 eV, respectively, using UPS, as shown in Figure S18 (Supporting Information). Combined with their optical bandgaps (Figure S19, Supporting Information), the CBMs of the control and NH_4SCN perovskite films were calculated to be −3.13 and −3.23 eV, respectively.

The current density-voltage-luminance (J-V-L) curves show that the NH_4SCN device has a lower turn-on voltage (2.6 V) compared to the control device (2.7 V) (Figure 4c), which may be

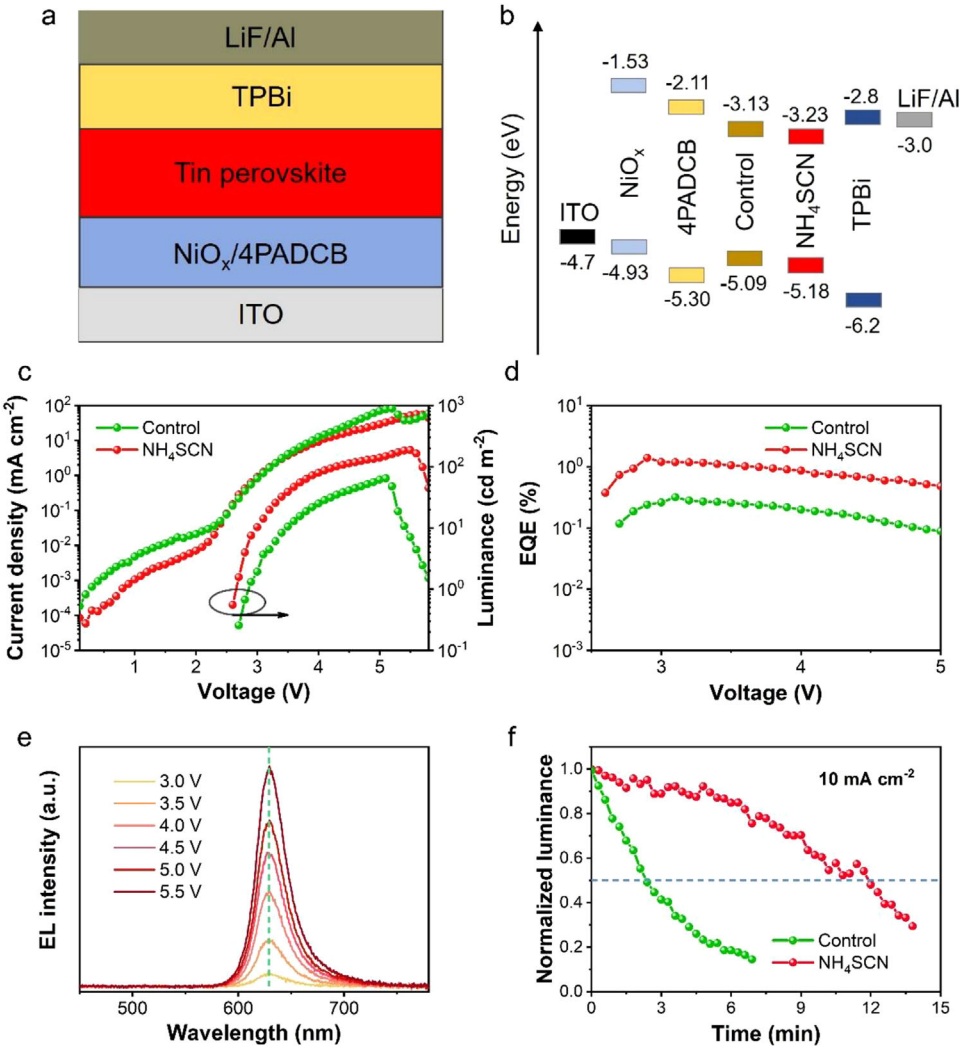

Figure 4. Device performance of PEA_2SnI_4 PeLEDs with or without NH_4SCN. a) Schematic device structure. b) Energy level diagram. c) Current density and luminance curves of the PeLEDs as a function of the applied voltage bias. d) External quantum efficiency-voltage (EQE-V) curves of the PeLEDs. e) Electroluminescence spectra of the PeLED with NH_4SCN. f) Operational stability of the PeLEDs with and without NH_4SCN.

attributed to better energy level alignment with 4PADCB and a lower trap density in the NH_4SCN films. Additionally, the maximum luminance of the NH_4SCN PeLED reaches 186.4 cd m^{-2}, nearly three times higher than that of the control PeLED (64.6 cd m^{-2}). EQE-V curves indicate that the NH_4SCN device achieves a peak EQE of 1.39% (Figure 4d), considerably higher than that of the control device (0.32%), which illustrates that the perovskite film obtained using the NH_4SCN additive enhances radiative recombination. A statistical distribution of peak EQE of the tin PeLEDs is shown in Figure S20 (Supporting Information). The average peak EQE of the NH_4SCN devices (NH_4SCN:SnI_2 = 0.2:1) is 0.81%, representing a fourfold enhancement compared to that of the control devices (0.19%), and a twofold increase relative to the NH_4SCN devices (NH_4SCN:SnI_2 = 0.1:1). When the NH_4SCN:SnI_2 ratio is increased to 0.5:1, the average peak EQE of the NH_4SCN devices (NH_4SCN:SnI_2 = 0.5:1) decreases to 0.24%. Although this approach shows promise in reducing the efficiency gap between DMSO-free and DMSO-contained tin-based PeLEDs, the overall performance still lags behind. Further improvement could be achieved via slowing down the crystallization process, suppressing interfacial non-radiative recombination, and keeping charge injection balance. The NH_4SCN PeLED also exhibited good electroluminescence (EL) stability, with a peak wavelength at 629 nm remaining unchanged as the drive voltage increased (Figure 4e). The corresponding Commission Internationale de L'Eclairage (CIE) coordinates are (0.683, 0.302) (Figure S21, Supporting Information), indicating a high color-purity red emission.[6,10]

Furthermore, operational stability tests were conducted for the tin PeLEDs at a constant current density of 10 mA cm^{-2} in a N_2-filled glovebox. The NH_4SCN PeLED demonstrated an operating half-life time (T_{50}) more than four times that of the control device (11.8 min vs 2.8 min) (Figure 4f). This enhancement may be attributed to the reduced traps, suppressed Sn(II) oxidation, and improved tin perovskite film quality. Figure S22 (Supporting Information) contains a photograph of the Al electrode before

and after the operational stability testing. Before the test, the Al electrode has a metallic luster with a high reflectivity. However, after applying bias during the device stability test, the Al electrode lost its metallic luster and turned whitish, suggesting Al degradation and morphological changes in the Al cathode, consistent with other studies.[41] The degradation may be attributed to the presence of residual moisture and/or oxygen in the glovebox, as well as ion migration under bias voltage.[41,42,43,44] Therefore, improving the stability of the Al cathode is essential to achieving the long-term operational stability of PeLEDs.

3. Conclusion

This study demonstrates that employing NH_4SCN as an additive in a DEF/DMPU-based PPS affords high quality Sn-based perovskite films, that when integrated with a NiO_x/SAM hole transport material affords efficient and stable lead-free perovskite-based PeLEDs. The NH_4SCN additive slows crystallization of the perovskite film as the SCN^- anion coordinates to the Sn^{2+} center, as demonstrated by NMR spectroscopy. This interaction also helps to stabilize the Sn^{2+} center, impeding oxidation to Sn^{4+}. The resulting improved film crystallinity and reduced defects enhance radiative recombination, resulting in PeLEDs with superior EQEs and operational stability compared to the control devices.

Supporting Information

Supporting Information is available from the Wiley Online Library or from the author.

Acknowledgements

The authors acknowledge financial support from the Valais Energy Demonstrators fund, EPFL Valais-Wallis, and HESSO. B. Z. acknowledges financial support from the Novo Nordisk Foundation (NNF24OC0094858). The authors thank Dr. Pascal A. Schouwink for measuring GIWAXS data. Computing resources used in this work were provided by the National Center for High Performance Computing of Turkiye (UHeM). The authors thank Dr. Mounir Driss Mensi for discussing XPS data fitting.

Conflict of Interest

The authors declare no conflicts of interest.

Author Contributions

S.T., M.K.N., and P.J.D. conceived this project. M.K.N., and P.J.D. supervised the project. S.T. designed the experiments, fabricated devices, and carried out films and devices characterization. O.N., P.U.J., and B.Z. performed THz spectroscopy measurements and data analysis. I.Y. performed DFT calculations. Y.L., S.Z., E.U., and A.A. performed in situ PL measurements. S.T. wrote the first draft of the paper. All authors revised the paper.

Data Availability Statement

The data that support the findings of this study are available in the supplementary material of this article.

Keywords

crystallization modulation, defect passivation, DMSO-free, PeLEDs, tin-based perovskite

Received: November 14, 2025
Published online: December 30, 2025

[1] Z.-K. Tan, R. S. Moghaddam, M. L. Lai, P. Docampo, R. Higler, F. Deschler, M. Price, A. Sadhanala, L. M. Pazos, D. Credgington, F. Hanusch, T. Bein, H. J. Snaith, R. H. Friend, *Nat. Nanotechnol.* **2014**, *9*, 687.
[2] C. Kuang, Z. Hu, Z. Yuan, K. Wen, J. Qing, L. Kobera, S. Abbrent, J. Brus, C. Yin, H. Wang, W. Xu, J. Wang, S. Bai, F. Gao, *Joule* **2021**, *5*, 618.
[3] Y. Cao, N. Wang, H. Tian, J. Guo, Y. Wei, H. Chen, Y. Miao, W. Zou, K. Pan, Y. He, H. Cao, Y. Ke, M. Xu, Y. Wang, M. Yang, K. Du, Z. Fu, D. Kong, D. Dai, Y. Jin, G. Li, H. Li, Q. Peng, J. Wang, W. Huang, *Nature* **2018**, *562*, 249.
[4] K. Wei, T. Zhou, Y. Jiang, C. Sun, Y. Liu, S. Li, S. Liu, X. Fu, C. Hu, S. Tian, Y. Yang, X. Fu, N. AlMasoud, S. M. H. Qaid, M. K. Nazeeruddin, H.-Y. Hsu, W.-D. Li, J. T. Kim, R. Long, W. Zhang, J. Chen, M. Yuan, *Nature* **2025**, *638*, 949.
[5] Y. Hassan, J. H. Park, M. L. Crawford, A. Sadhanala, J. Lee, J. C. Sadighian, E. Mosconi, R. Shivanna, E. Radicchi, M. Jeong, C. Yang, H. Choi, S. H. Park, M. H. Song, F. De Angelis, C. Y. Wong, R. H. Friend, B. R. Lee, H. J. Snaith, *Nature* **2021**, *591*, 72.
[6] S. Tian, G. Li, R. C. Turnell-Ritson, Z. Fei, A. Bornet, M. K. Nazeeruddin, P. J. Dyson, *Angew Chem.* **2024**, *136*, 202407193 .
[7] M. I. Saidaminov, I. Spanopoulos, J. Abed, W. Ke, J. Wicks, M. G. Kanatzidis, E. H. Sargent, *ACS Energy Lett.* **2020**, *5*, 1153.
[8] B. Chen, Z. Yu, A. Onno, Z. Yu, S. Chen, J. Wang, Z. C. Holman, J. Huang, *Sci. Adv.* **2022**, *8*, add0377.
[9] H. Jia, H. Shi, R. Yu, H. Ma, Z. Wang, C. Zou, Z. Tan, *Small* **2022**, *18*, 2200036.
[10] D. Han, J. Wang, L. Agosta, Z. Zang, B. Zhao, L. Kong, H. Lu, I. Mosquera-Lois, V. Carnevali, J. Dong, J. Zhou, H. Ji, L. Pfeifer, S. M. Zakeeruddin, Y. Yang, B. Wu, U. Rothlisberger, X. Yang, M. Grätzel, N. Wang, *Nature* **2023**, *622*, 493.
[11] F. Yuan, X. Zheng, A. Johnston, Y.a-K. Wang, C. Zhou, Y. Dong, B. Chen, H. Chen, J. Z. Fan, G. Sharma, P. Li, Y. Gao, O. Voznyy, H.-T. Kung, Z.-H. Lu, O. M. Bakr, E. H. Sargent, *Sci. Adv.* **2020**, *6*, abb0253. .
[12] Y. Meng, X. Guan, Y. Weng, J. Lu, Y. Li, Y. Zhao, M. Li, W. Feng, C. Sun, J. Lin, Z. Wei, *Adv. Funct. Mater.* **2023**, *34*, 2310530.
[13] H. Min, J. Chang, Y. Tong, J. Wang, F. Zhang, Z. Feng, X. Bi, N. Chen, Z. Kuang, S. Wang, L. Yuan, H. Shi, N. Zhao, D. Qian, S. Xu, L. Zhu, N. Wang, W. Huang, J. Wang, *Nat. Photonics* **2023**, *17*, 755.
[14] J. Zhu, C. Ge, B. Jiang, X. Zhang, J. Luo, J. Tang, *Adv. Funct. Mater.* **2025**, *35*, 2506504.
[15] S. Wang, X. Zhang, W. Zhu, Z. Tang, J. Liu, H. Zhang, L. Ding, F. Hao, *Appl. Surf. Sci.* **2022**, *602*, 154393.
[16] J. Chen, J. Li, R. Pau, L. Chen, M. Kot, H. Wang, L. D. Mario, G. Portale, M. A. Loi, *Adv. Mater.* **2024**, *37*, 2415958 .
[17] W. Gao, R. Huang, H. Dong, W. Li, Z. Wu, Y. Chen, C. Ran, *Chem. Soc. Rev.* **2024**, *54*, 1384.
[18] T. Nakamura, S. Yakumaru, M. A. Truong, K. Kim, J. Liu, S. Hu, K. Otsuka, R. Hashimoto, R. Murdey, T. Sasamori, H. D. Kim, H. Ohkita, T. Handa, Y. Kanemitsu, A. Wakamiya, *Nat. Commun.* **2020**, *11*, 3008.

[19] X. Jiang, H. Li, Q. Zhou, Q. Wei, M. Wei, L. Jiang, Z. Wang, Z. Peng, F. Wang, Z. Zang, K. Xu, Y. Hou, S. Teale, W. Zhou, R. Si, X. Gao, E. H. Sargent, Z. Ning, *J. Am. Chem. Soc.* **2021**, *143*, 10970.
[20] H. Min, N. Wang, N. Chen, Y. Tong, Y. Wang, J. Wang, J. Liu, S. Wang, X. Wu, P. Yang, H. Shi, C. Zhuo, Q.i Chen, J. Li, D. Zhang, X. Lu, C. Zhu, Q. Peng, L. Zhu, J. Chang, W. Huang, J. Wang, *Nat. Nanotechnol.* **2024**, *19*, 632.
[21] J. Pascual, D. Di Girolamo, M. A. Flatken, M. H. Aldamasy, G. Li, M. Li, A. Abate, *Chemistry* **2022**, *28*, 202103919.
[22] D. Di Girolamo, J. Pascual, M. H. Aldamasy, Z. Iqbal, G. Li, E. Radicchi, M. Li, S.-H. Turren-Cruz, G. Nasti, A. Dallmann, F. De Angelis, A. Abate, *ACS Energy Lett.* **2021**, *6*, 959.
[23] Z. Li, X. Li, M. Wang, M. Cai, X. Shi, Y. Mo, X. Chen, D. Ren, M. Yang, X. Liu, R. Jia, N. V. Medhekar, S. Dai, *ACS Appl. Energy Mater.* **2021**, *5*, 108.
[24] C. R. D. Yukta, P. Yadav, S. Satapathi, *ACS Appl. Energy Mater.* **2022**, *5*, 13723.
[25] F. Wang, X. Jiang, H. Chen, Y. Shang, H. Liu, J. Wei, W. Zhou, H. He, W. Liu, Z. Ning, *Joule* **2018**, *2*, 2732.
[26] H. Duim, A. J. Rommens, S. Shao, G. Portale, M. A. Loi, *ACS Appl. Energy Mater.* **2023**, *6*, 10285.
[27] N. Guo, J. Li, S. Yang, J. Zhang, J. Ni, H. Cai, *Nanotechnology* **2021**, *32*, 395704.
[28] S. Tian, X.-X. Gao, D. Reyes, O. A. Syzgantseva, M. M. Baytemirov, N. Shibayama, H. Kanda, P. A. Schouwink, Z. Fei, L. Zhong, F. F. Tiranito, Y. Fang, P. J. Dyson, M. K. Nazeeruddin, *Small* **2024**, *20*, 2406929.
[29] M. Pitaro, L. Di Mario, J. Pinna, D. A. Acevedo-Guzmán, M. Neophytou, M. Kirkus, T. D. Anthopoulos, G. Portale, P. Rudolf, M. A. Loi, *Carbon Energy* **2025**, *7*, 710.
[30] T. B. Song, Z. Yuan, M. Mori, F. Motiwala, G. Segev, E. Masquelier, C. V. Stan, J. L. Slack, N. Tamura, C. M. Sutter-Fella, *Adv. Funct. Mater.* **2019**, *30*, 1908337.
[31] S. Zuo, A. Tarasov, L. Frohloff, K. Prashanthan, F. Ruske, M. Lounasvuori, C. Frasca, A. Dallmann, F. Zu, F. Mathies, F. Scheler, N. T. P. Hartono, G. Li, J. Li, M. Simmonds, W. Li, N. Koch, S. Albrecht, M. Li, E. Unger, M. H. Aldanmasy, A. Musiienko, A. Abate, *Adv. Sci. (Weinh)* **2025**, 01311.
[32] H. Rao, Y. Su, G. Liu, H. Zhou, J. Yang, W. Sheng, Y. Zhong, L. Tan, Y. Chen, *Angew Chem. Int. Ed. Engl.* **2023**, *62*, 202306712.
[33] C. Wehrenfennig, G. E. Eperon, M. B. Johnston, H. J. Snaith, L. M. Herz, *Adv. Mater.* **2014**, *26*, 1584.
[34] J. A. Spies, J. Neu, U. T. Tayvah, M. D. Capobianco, B. Pattengale, S. Ostresh, C. A. Schmuttenmaer, *J. Phys. Chem. C* **2020**, *124*, 22335.
[35] M. K. Sørensen, A. S. Gertsen, R. P. Fornari, B. Zhou, X. Zhang, P. U. Jepsen, E. Stanzani, S. Yun, M. F. Castro, M. Schwartzkopf, A. Koutsioubas, P. de Silva, M. Espindola-Rodriguez, L. T. Kuhn, J. W. Andreasen, *Adv. Funct. Mater.* **2023**, *33*, 2212835 .
[36] E. K. Tekelenburg, F. V. A. Camargo, A. Filippetti, A. Mattoni, L. J. M. van de Ven, M. Pitaro, G. Cerullo, M. A. Loi, *Adv. Mater.* **2025**, *37*, 2411892.
[37] D. G. Cooke, F. C. Krebs, P. U. Jepsen, *Phys. Rev. Lett.* **2012**, *108*, 056603.
[38] M. Pitaro, E. K. Tekelenburg, S. Shao, M. A. Loi, *Adv. Mater.* **2022**, *34*, 2105844 .
[39] Y. Zhou, Y. Zhou, X. Huang, J. Zhang, L. Zhang, H. Wu, Y. Zhou, Y. Wang, Y. Wang, W. Fu, H. Chen, *Adv. Energy Mater.* **2024**, *14*, 2400616.
[40] C. Li, Y. Chen, Z. Zhang, C. Liu, F. Guo, W. Ahmad, P. Gao, *Energy Environ. Sci.* **2024**, *17*, 6157.
[41] T. H. Do, A. Loganathan, Y. F. Yin, X. Y. Lin, Y. S. Fu, T. F. Guo, *Adv. Funct. Mater.* **2025**, https://doi.org/10.1002/adfm.202521392.
[42] V. Prakasam, D. Tordera, H. J. Bolink, G. Gelinck, *Adv. Opt. Mater.* **2019**, *7*, 1900902.
[43] Y. Zou, T. Wu, F. Fu, S. Bai, L. Cai, Z. Yuan, Y. Li, R. Li, W. Xu, T. Song, Y. Yang, X. Gao, F. Gao, B. Sun, *J. Mater. Chem. C* **2020**, *8*, 15079.
[44] H. Lee, D. Ko, C. Lee, *ACS Appl. Mater. Interfaces* **2019**, *11*, 11667.